Alex Fromholtz
Department of Biomedical Engineering,
Rutgers University,
Piscataway, NJ 08854
e-mail: afromholtz@gmail.com

Max L. Balter[1]
Department of Biomedical Engineering,
Rutgers University,
Piscataway, NJ 08854
e-mail: balterm53@gmail.com

Alvin I. Chen
Department of Biomedical Engineering,
Rutgers University,
Piscataway, NJ 08854
e-mail: alv6688@gmail.com

Josh M. Leipheimer
Department of Biomedical Engineering,
Rutgers University,
Piscataway, NJ 08854
e-mail: joshleiph@gmail.com

Anil Shrirao
Department of Biomedical Engineering,
Rutgers University,
Piscataway, NJ 08854
e-mail: anilshrirao@gmail.com

Timothy J. Maguire
Department of Biomedical Engineering,
Rutgers University,
Piscataway, NJ 08854
e-mail: timjm@rutgers.edu

Martin L. Yarmush
Paul and Mary Monroe Distinguished Professor
Department of Biomedical Engineering,
Rutgers University,
Piscataway, NJ 08854
e-mail: yarmush@rci.rutgers.edu

Design and Evaluation of a Robotic Device for Automated Tail Vein Cannulations in Rodent Models

Preclinical testing in rodent models is a ubiquitous part of modern biomedical research and commonly involves accessing the venous bloodstream for blood sampling and drug delivery. Manual tail vein cannulation is a time-consuming process and requires significant skill and training, particularly since improperly inserted needles can affect the experimental results and study outcomes. In this paper, we present a miniaturized, robotic medical device for automated, image-guided tail vein cannulations in rodent models. The device is composed of an actuated three degrees-of-freedom (DOFs) needle manipulator, three-dimensional (3D) near-infrared (NIR) stereo cameras, and an animal holding platform. Evaluating the system through a series of workspace simulations and free-space positioning tests, the device exhibited a sufficient work volume for the needle insertion task and submillimeter accuracy over the calibration targets. The results indicate that the device is capable of cannulating tail veins in rodent models as small as 0.3 mm in diameter, the smallest diameter vein required to target.
[DOI: 10.1115/1.4038011]

1 Introduction

Accessing the venous bloodstream of rodent models for drug delivery or blood sampling is often required for studying biological genotypes [1], performing molecular imaging [2], or injecting cells [3] or therapeutics [4]. In each case, repeatable, accurate needle insertion plays a key role in driving reliable results [5]. Poorly inserted needles can lead to high levels of variability and potentially erroneous test results in animal studies. Additionally, improperly placed needles can result in damage to the vessel and surrounding tissue structure, pain, and trauma to the animal, and lengthened time to complete the procedure [6].

Traditionally, the needle insertion is performed manually by hand, where success rates depend on technical skill [2]. The most common vein used for needle insertion in rodents is the lateral tail vein, which for a typical lab mouse and rat is approximately 0.3 and 0.5 mm in diameter, respectively [7,8]. Due to the small size of the vessels, oftentimes, they are difficult to localize and puncture. For example, in an experiment performed by Groman and Reinhardt [9], three trained technicians were each tasked with injecting ten different mice with colloidal gold. Out of 30 injections, ten were deemed mis-administered. Moreover, only 1 out of 30 injections was deemed qualitatively poor at first, before being quantified via imaging for proper dispersion of injected volume within the tail. This finding suggests that a technician may be unaware of whether the needle insertion was successful.

Additionally, any sudden animal movement due to initial needle insertion and vasoconstriction of veins from anesthesia can increase difficulty in accurate needle insertion [10,11]. Steps may be taken during the animal preparation can include soaking the tail in warm water, using a chamber to raise the body temperature, or physically restraining the animal [10,12]. However, these methods are time consuming, can introduce experimental variability, and do not always result in improved cannulation success rates.

Imaging systems, such as X-ray computed tomography, magnetic resonance imaging, near infrared (NIR), and ultrasound, have shown promise for assisting technicians in visualizing small animal vessels [6,13]. However, manual needle insertion remains a challenging procedure, requiring a high degree of dexterity and visuomotor coordination.

Recently, several robotic systems have been developed for automated venipuncture in rodent models [14,15]. These devices

[1]Corresponding author.

Manuscript received April 13, 2017; final manuscript received September 14, 2017; published online October 16, 2017. Assoc. Editor: Carl Nelson.

combine the benefits of an imaging modality to enhance vein detection with robotics to accurately introduce the needle into the target vessel. For example, Waspe et al. designed a robotic needle positioning system for image-guided interventions in small animals [16]. This system utilized two rotational and one linear degree-of-freedom (DOF) to manipulate the needle position and orientation about a remote center of motion. Needle positioning testing for this remote center of motion-based device resulted in a free space accuracy of 54±12 μm and 91±21 μm for the pitch and roll axis, respectively. However, robot calibration was time consuming (i.e., over 1 h) requiring an average of five to six calibration iterations per axis. Additionally, these calibrations were dependent on the cannula, meaning recalibration is necessary when replacing the needle. As another example, Ayadi et al. developed a system which combines a 6DOF robotic arm with a structured light imaging unit for three-dimensional (3D) visualization [17]. Position testing resulted in an accuracy of <0.5 pixels for the needle tip and 0.06 deg for the needle direction control. This system also required a separate, bulky structure for mounting the imaging components.

Despite the promising results in these studies, these prototype systems are relatively large and rely on complex mechanisms for needle positioning and insertion. Due to the large footprints, it would be challenging to run multiple devices simultaneously in a lab for the purpose of expediting preclinical testing. Furthermore, both systems require a lengthy and complex process to setup for animal testing.

To overcome these limitations, our group is developing a miniaturized and compact robotic device for automated tail vein insertions in rodent models, as pictured in Fig. 1. Using only 3DOF, the system is able to rotate 180 deg about the circumference of the tail to identify subcutaneous vessels, automatically select the optimal point of insertion, and then introduce a needle into the target vein. Three-dimensional NIR stereo imaging is used to localize veins and precisely control needle positioning, while a holding platform is used to ensure that the tail and animal remain fixed during the procedure. As seen with the development of a venipuncture device for humans, we hypothesize that this system will yield both an increase in accuracy and a decrease in procedure time [18]. Our target accuracy requirement is a 0.3 mm tail vein diameter—the smallest diameter of a mouse tail vein.

In this paper, we describe the mechanical designs of the device and evaluate the positioning accuracy of the needle manipulator. Sections 2.1–2.3 of this paper break down the device into its three main components: (1) the needle manipulator assembly, (2) imaging unit, and (3) animal-holding platform. We then analyze the workspace and kinematics of the device and perform a series of free-space positioning studies to evaluate accuracy, precision, and repeatability.

2 Device Design

Key factors to consider when choosing a vein for cannulation include vein accessibility, size, and visibility. These can vary for different rodent models depending on skin pigmentation, internal tissue structures, and species [9,10]. Other physical variables such as sudden animal movements or vasoconstriction due to bodily heat loss can further complicate the procedure [10,19]. Our system addresses these factors by using 3D NIR imaging coupled with a robotic needle manipulator to ensure precise needle control and improved insertion accuracy. Additionally, the system includes a physical restraint for the animal, reducing unpredictable motion without inducing unnecessary trauma.

Due to the small size of the device (i.e., 33 cm × 10 cm × 5 cm), a testing facility could use multiple devices in parallel to expedite throughput of tail vein punctures. Due to the unique mechanism combinations on the device, the needle manipulator and imaging components need only 3DOF for 180 deg of rotational freedom about the tail center when localizing insertion points. The device is comprised of three main components, each described in the following sections: needle manipulator assembly (Sec. 2.1), imaging unit (Sec. 2.2), and animal-holding platform (Sec. 2.3).

2.1 Needle Manipulator Assembly. Both the needle manipulator and the imaging unit are seated on a custom-designed friction gear ring, laser cut from a 1/4 in cast acrylic sheet. This configuration ensures that the imaging unit maintains an optimal field of view with respect to the needle insertion point and the tail of the animal. The rotating ring utilizes a friction gear mechanism to grant the 180 deg angle approach on the topside of the tail, as shown in Fig. 2(*a*). Detection of veins with this approach enables the device to inject either the dorsal or lateral vein. The friction gear, modeled after a hollow ring gear, was implemented because of lower backlash, compared to a spur gear drivetrain. Friction gears also carry other beneficial features, such as backdrivability, as well as protecting the motors, which contain rigid gearheads. The degree in which the rubber drive wheel attached to the motor is pressed into the friction gear is also adjustable, allowing for controlled variability of the force threshold for slip. Additionally, fine teeth (0.5 mm × 0.5 mm) were cut on the outside edge of the friction gear to reduce slip. The manipulator is mounted to the friction gear using a linear slider (McMaster-Carr, PN: 8381K290) and a vertical alignment attachment, as shown in Fig. 2. These work tangentially with an adjusted rack and pinion setup (designs adapted from Stock Drive Products and Sterling Instrument, Hicksville, NY) to allow for smooth vertical motion of the manipulator. A positioning plug ensures that the helical pinion rotates along its longitudinal axis, whereas adjustable screws can be used to control teeth-meshing of the rack and pinion. Both the main rack of the needle manipulator and the helical pinion used for vertical movement are designed to maintain a fixed

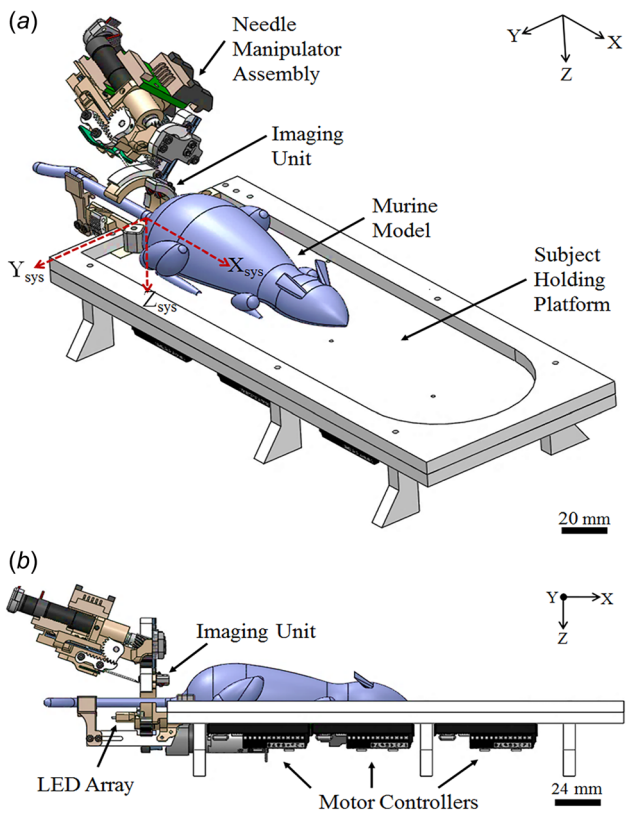

Fig. 1 Design of the robotic device for automated tail vein insertions in rodent models: (*a*) isometric view illustrating the needle manipulator assembly, imaging unit, rodent model, and animal holding platform and (*b*) side view of the device highlighting the imaging unit, LED array and motor controllers hidden under the holding platform

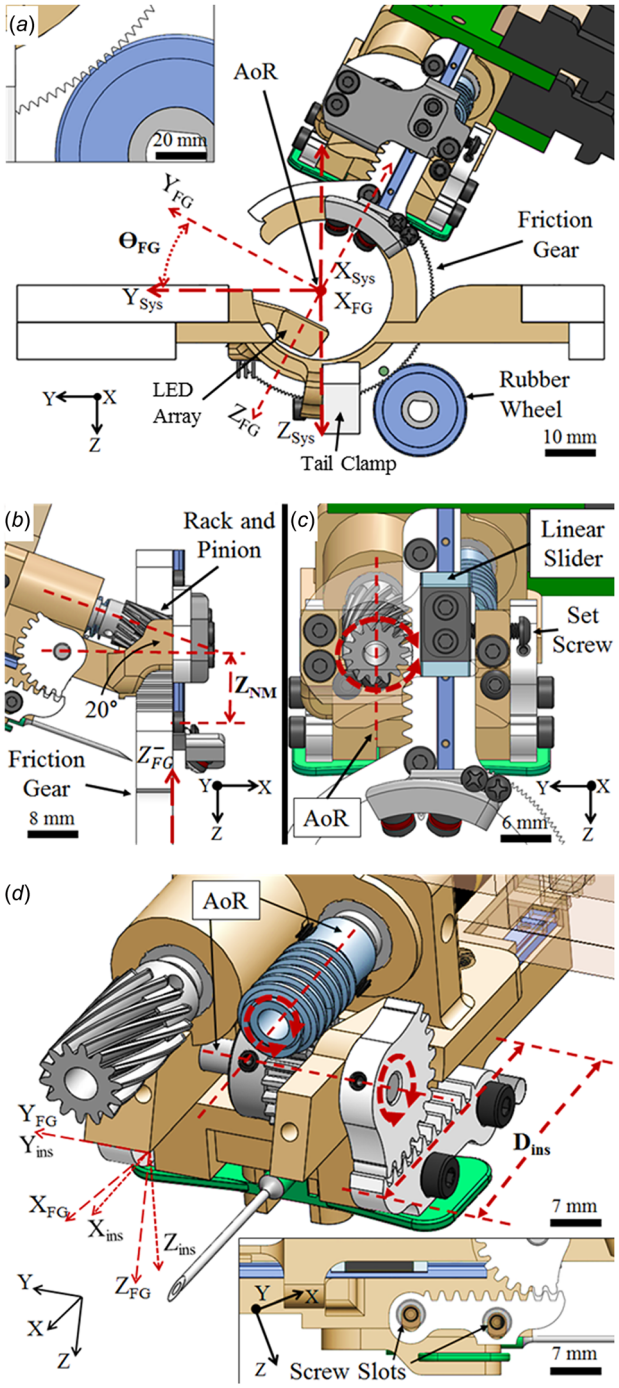

Fig. 2 Depiction of the three degrees of motion. (*a*) θ_{FG} and its relative coordinate frame on the holding platform. The axis of rotation is denoted as AoR. Additional components such as the light-emitting diode (LED) array and the tail clamp arm are also labeled. (*b*) Side and (*c*) front view of Z_{NM}. This DOF is achieved using a rack and pinion mechanism with a helical pinion at 2 deg to align the motors with the insertion angle. (*d*) D_{ins} and its chain of mechanisms linked together, which directly controls the needle insertion, and allows the needle path to remain parallel to the drive motor axle. Inset shows the slot design for finer control over mechanism backlash.

20 deg needle insertion angle. After consulting with numerous lab technicians, this angle was determined to be optimal for vein cannulation.

For the needle insertion degree of motion, a chain of mechanisms (as shown in Fig. 2(*d*)) was designed combining a worm, worm gear, drive axle, and rack/pinion system (designs adapted from Stock Drive Products and Sterling Instrument, Hicksville, NY). This allowed for the centering and realignment of the motor with respect to the center of mass on the needle manipulator. To compensate for backlash in the mechanism, the following modifications were implemented. The rack and pinion gears were laser cut from acrylic and included slots instead of screw holes to provide better control over teeth-meshing depth. The worm and spur gears were also rapid prototyped to ensure precise fabrication of the customized components. The needle (Harvard Apparatus winged infusion needle, 25G, 19 mm length) sits in a disposable adapter that allows for easy attachment and removal from the manipulator by use of an embedded magnet. Quick and easy decoupling of the needle from the robot is important to minimize manipulation of the tail before injecting or aspirating fluids with a syringe. The needle reported in this paper—0.51 mm in diameter—is suitable for cannulation in both rats and mice. The system can easily be adapted to other needle diameters and lengths, or to precision syringes (e.g., Hamilton syringes) by interchanging different needle adapters.

In total, these three degrees of motion give the system approximately 1600 mm^3 of workspace in which it can position a needle for successful tail vein cannulation. While the first DOF (θ_{FG}) uses a 16-mm-diameter DC brushed motor assembly (Maxon Precision Motors, RE-16), the second and third DOF (Z_{NM}, D_{ins} respectively) use 10-mm-diameter DC brushed motor assemblies (Maxon Precision Motors, RE-10). Gearheads and encoders for the motor assemblies were chosen to ensure precise motion control and needle positioning. Table 1 lists the gear ratios, encoder counts per revolution, and resolution for each motor in the system. Mechanism gear ratios per DOF were derived from calculations specific to each axis-of-motion and their respective external gearing mechanism. Despite the high resolution in the motor assemblies, there is inherent backlash in the gearheads and external gearing mechanisms resulting in a slight reduction in the reported resolution. Finally, all the motor controllers are housed underneath the platform. Each DOF is controlled by individual motor drivers (Maxon Precision Motors, EPOS2). Using a USB2CAN communication protocol, these motor drivers are daisy-chained in a master-slave control network. The master console is connected to the host processor via USB (1 MB/s transfer rate), while transmit and receive signals are sent between the master and slave devices.

2.2 Imaging Unit. The imaging unit is mounted to the rotating friction gear ring for an eye-in-hand configuration. This unit contains miniaturized NIR cameras (VRMagic, PN: VRmMS-12) angled 40 deg and 10 deg ($\theta_{FG\text{-}ZX}$ and $\theta_{FG\text{-}ZY}$) with respect to the friction gear coordinate frame, as shown in Fig. 3(*b*), to ensure the vessel and needle remain in the field of view throughout the procedure. Stereo cameras are used for 3D visualization of the tissue and needle. Fixated on the bottom of the rotating friction gear across from the cameras is an array of LEDs (760 nm and 940 nm). The LED configuration enables transillumination through the tail, providing constant light without concern for change in θ_{FG}, as the friction gear rotates. In this fashion, transmitted light from underneath the tail is captured by the cameras above to provide internal tissue structure imaging.

Table 1 Motor parameters for each degree of motion

DOF	θ_{FG}	Z_{NM}	D_{ins}
Motor diameter (mm)	16	10	10
Gearhead ratio	84:1	64:1	64:1
Encoder count (cpt)	512	512	512
Resolution (deg/ct)	0.0021	0.0055	0.0055
Mechanism gear ratio	2.3:1	25.1:1	2.4:1

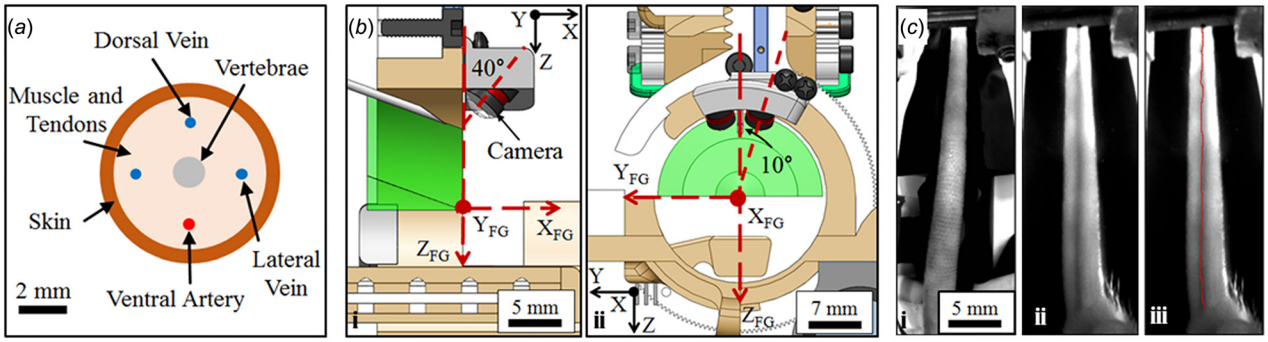

Fig. 3 Key components of the imaging system: (*a*) cross-sectional illustration of a rodent tail anatomy, (*b*) front (i) and side (ii) views of the imaging unit, with labeled camera angles, and (*c*) NIR tail vein imaging and segmentation. Image acquired under visible light (i), corresponding image acquired with the NIR imaging system using the transillumination method (ii), and tail vein segmentation applied to the NIR image (iii).

Near-infrared imaging is optimal for visualizing blood vessels, specifically veins, due to reduced scatter of NIR light on the skin surface and increased hemoglobin absorption in veins [18]. Images are captured by the cameras and sent to the host processor for analysis. A compact PC (ASUS Intel Core i7-4720HQ) in conjunction with a graphics card (NVIDIA Quadro M4000) was utilized for the experiments conducted in this study. In this setup, the graphics processor handles the image processing routines, whereas the central processing unit handles the robotic kinematic controls and user interface. Software for the kinematics, motion control, and image processing was written in LabVIEW.

Stereo vision techniques are applied to compute the 3D position of a cannulation target on the lateral tail vein of the animal. The pair of NIR cameras were calibrated in an offline manner using an independent motorized Cartesian stage and a rectilinear pattern grid with circular control points. In the calibration process, we first determined the internal parameters of each camera to correct for geometric distortions; we then solved for the projective mapping that transforms the original image pair into a rectified image pair [20]. Once calibrated, the cameras were fixed in place and mounted to the device.

During the procedure, the device uses the NIR stereo cameras to scan for the lateral veins running along the tail. We applied vessel enhancement and segmentation algorithms, as described in Chen et al. [18], to extract the centerlines of the vessels with subpixel accuracy. Since there are only two lateral veins in the tail, the stereo reconstruction problem is reduced to identifying corresponding points of the segmented vessels along the horizontal epipolar lines of the rectified image pairs. This approach substantially simplifies the 3D localization process compared to standard methods of stereo correspondence on raw intensity images, and dramatically reduces the computational effort. The 3D coordinate of the selected cannulation target is relayed to the manipulator based on the known camera-to-robot registration transformation. Uncertainty in the co-registration transform is minimized using the free-space calibration routine described in Balter et al. [21].

2.3 Animal-Holding Platform. The platform functions as a restraint for the animal and provides structure to the full device. The rotating friction gear rotates about the center of the tail channel on the main gear plate, as illustrated in Fig. 2(*a*). This plate bridges the platform to the rotating gear and therefore the needle manipulator and imaging unit.

To reduce animal movement during needle insertion, the holding platform includes tail clamps and a bumper to steady the base of the tail. The clamps are positioned to apply pressure approximately two-thirds down the length of the tail from the base, enhancing visibility of the veins, as shown in Fig. 1(*b*). A heated pad (Kent-Scientific, PN: TPZ-814EA) on the animal-holding platform helps regulate the body temperature of the animal and reduce vasodilation within the extremities. The pad is maintained at a temperature of approximately 37–38 °C [11]. A disposable cover is placed over the pad to ensure sterility between test animals. Comprised mostly of 3D-printed acrylonitrile butadiene styrene plastic and laser-cut acrylic, the platform itself can be cleaned with alcohol wipes between procedures.

3 Experimental Results

The system was developed for highly accurate and repeatable needle positioning, with the capacity to cannulate vessels as small as 0.3 mm in diameter. To achieve this, we created a 3DOF robot that consisted of novel mechanisms to minimize backlash at the joints. Kinematics were derived based on the robot geometry to correlate joint frames in the needle manipulator. Using the kinematic equations, free-space positioning experiments were conducted on a simulated rat tail (i.e., a cylindrical test rig with uniformly spaced calibration dots) in which the robot positioned the needle tip on the surface of the test rig. As noted in Fig. 4, the global *z*-axis of the device points downward. This is done to create a coordinate frame in which the needle insertion is a positive motion.

3.1 Workspace Analysis. Forward kinematics, Eqs. (1)–(3), were used to compute the needle tip position (X_N, Y_N, Z_N) based on a given set of joint angles (θ_{FG}, Z_{NM}, D_{ins})

$$X_N = D_{ins} \times \cos(20^\circ) \tag{1}$$

$$Y_N = \cot(\theta_{FG}) \times (Z_{NM} + D_{ins} \times \sin(20^\circ)) \tag{2}$$

$$Z_N = Z_{NM} + D_{ins} \times \sin(20^\circ) \tag{3}$$

Inverse kinematics were used to compute joint positions based on a desired needle tip position. There was only one unique solution in the inverse kinematics for a given needle tip position. The trigonometric calculations for the second and third degree of motion were based off the coordinate frames highlighted in Fig. 2(*b*). The origin of the animal-holding platform, as illustrated in Fig. 1, was also centered in the opening of the main gear plate component. Using these equations, we ran a series of kinematic simulations to determine the dexterous workspace of the robot. The needle tip, not the needle holder tray, was used for the calculations due to variability in needle lengths and gauges.

As illustrated in Fig. 4, the actual workspace was compared to the desired workspace to ensure the system could reach target points of insertion in the rodent tail. Additionally, the calibration cylinder was modeled to determine the robot's ability to place the needle tip at each of the desired calibration targets. The range of travel for each DOF was: ±90 deg for θ_{FG}, 8 mm for Z_{NM}, and

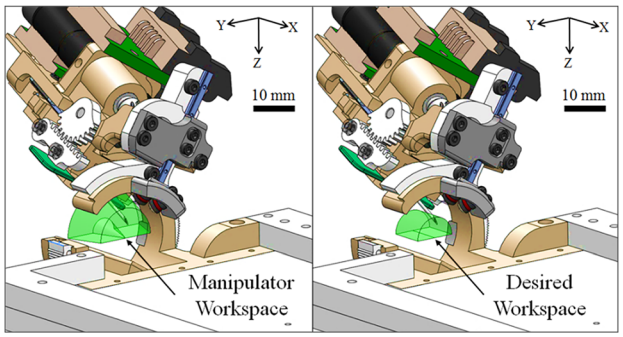

Fig. 4 Depiction of the actual (left) versus desired (right) workspace for the needle insertion task

8 mm for D_{ins}. These values were used to compute the dexterous workspace of the system: (1550 cm^3).

3.2 Position Testing. Using a cylindrical calibration model, free-space positioning experiments were performed to assess the accuracy and precision of the system within the operating workspace. A calibration rig comprised of 1 mm diameter circular targets uniformly spaced (1.8 mm center-to-center) over a cylindrical grid was used for the experiments, which was rigidly mounted to the device. The cylindrical calibration model was 4.6 mm in diameter, to mimic the diameter of a rat tail, with a grid pattern of 5×5 ($x \times y$, relative to the global coordinate frame in Fig. 1(*a*)). Figure 5(*b*) illustrates the location of the calibration target on the device.

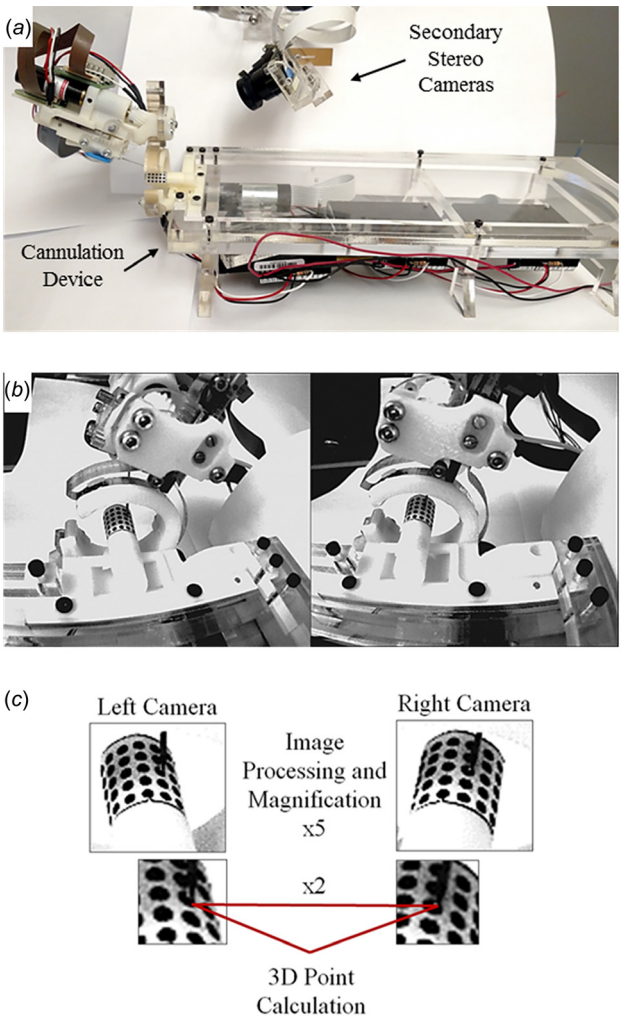

Fig. 5 Free-space needle positioning tests: (*a*) the experimental setup using the cylindrical calibration rig and a secondary set of stereo cameras situated above the device as labeled in the figure, (*b*) stereo images from the left and right cameras during testing, and (*c*) images magnified 5×, and the needle tip manually selected to compute the 3D position

To evaluate repeatability, ten positioning trials were conducted for each target, producing a total of 250 tests over the operating workspace of the robot. For each trial, the needle started in the home position; then, the device moved the needle tip to the desired circular target on the surface of the test rig. The system computed the desired joint angles required to position the needle tip at each target using the kinematic equations. Once the device completed the position move, images were acquired on the left and right cameras to compute the 3D location of the needle tip and circular target. Afterward, the device returned the needle to the home position before moving to the next location on the calibration model.

After the experiments, actual needle tip positions were compared against desired target locations to compute errors and standard deviations in the system. Desired target positions were obtained from the design model since the calibration cylinder was rigidly mounted to the device. To compute the actual needle tip positions, we used a second set of calibrated stereo vision cameras situated above the device, as shown in Fig. 5(*a*). These cameras were not mounted on the device and used for image guidance, but rather, were just used for the positioning trials.

Due to a slightly obstructed field of view of the calibration rig, needle positioning experiments were conducted within a range of ±70 deg on the θ_{FG} DOF. Positioning accuracy for the remaining θ_{FG} range can be extrapolated based on errors observed from testing at lower rotational angles. Figure 5(*c*) shows images from the left and right camera, with the needle tip positioned on the calibration target.

Images were analyzed after the experiments to obtain 3D position data using the following steps: First, the needle tip and circle target were manually extracted from each set of images, and their real-world positions were determined. The desired coordinates of the circular targets were extracted from the design model with each target defining a unique 3DOF pose (θ_{FG}, Z_{NM}, and D_{ins}). By computing the positioning error at each calibration target over the ten trials, accuracy and variation were obtained.

Averaging over the 25 targets and ten trials, root-mean-square errors were 0.157, 0.175, and 0.201 mm for *x*, *y*, and *z*, respectively. Meanwhile, the mean absolute errors were 0.126, 0.149, 0.152, and 0.355 mm for *x*, *y*, *z*, and magnitude, respectively. Table 2 summarizes the results from the experiments, highlighting the mean, maximum, standard deviation, and variability. The overall variability in the system was 0.17 mm—computed as the mean standard deviation of the needle tip position across all trials in *x* (0.148 mm), *y* (0.152 mm), and *z* (0.210 mm). The variability in the experimental setup (e.g., camera calibration) was 0.1 mm—computed as the mean standard deviation of the circle center position across the trials in *x* (0.065 mm), *y* (0.096 mm), and *z* (0.139 mm).

Table 2 Magnitude of errors and variability in needle positioning tests (25 targets; $n = 10$ trials). All units in millimeters.

	Mean	Max	StDev
Error magnitude	0.355	1.632	0.227
	X	*Y*	*Z*
Needle tip root-mean-square errors	0.157	0.175	0.201
Needle tip mean absolute errors	0.126	0.149	0.152
Needle tip S.D	0.148	0.152	0.210
Circle center S.D	0.065	0.096	0.139

Plotting the mean positioning errors in x, y, z, and magnitude, a series of error maps were generated across the operating workspace, as shown in Fig. 6. These error maps could then be applied to the system for calibration purposes, compensating for subtle inaccuracies in the construction of the robot, kinematics, and camera calibration. Specifically, by subtracting out these errors accordingly, calibrated offsets can be included in the motion control system to reduce needle positioning errors. Furthermore, motor servos in the device were monitored throughout the testing to ensure low errors between the desired and actual motor positions. This was done to investigate the source of errors during the needle positioning trials, which could arise due to low-level motor errors, mechanical instability, or camera calibration. Figure 7(*b*) displays plots comparing the desired versus actual signals of each motor. Actual positions were measured using the attached quadrature encoders on the back-end of the motors. Steady-state errors were 0.005 deg 0.01 mm, and 0.03 mm for θ_{FG}, Z_{NM}, and D_{ins}, respectively. Lag between commanded and actual positions could be reduced by increasing the movement speed of each joint.

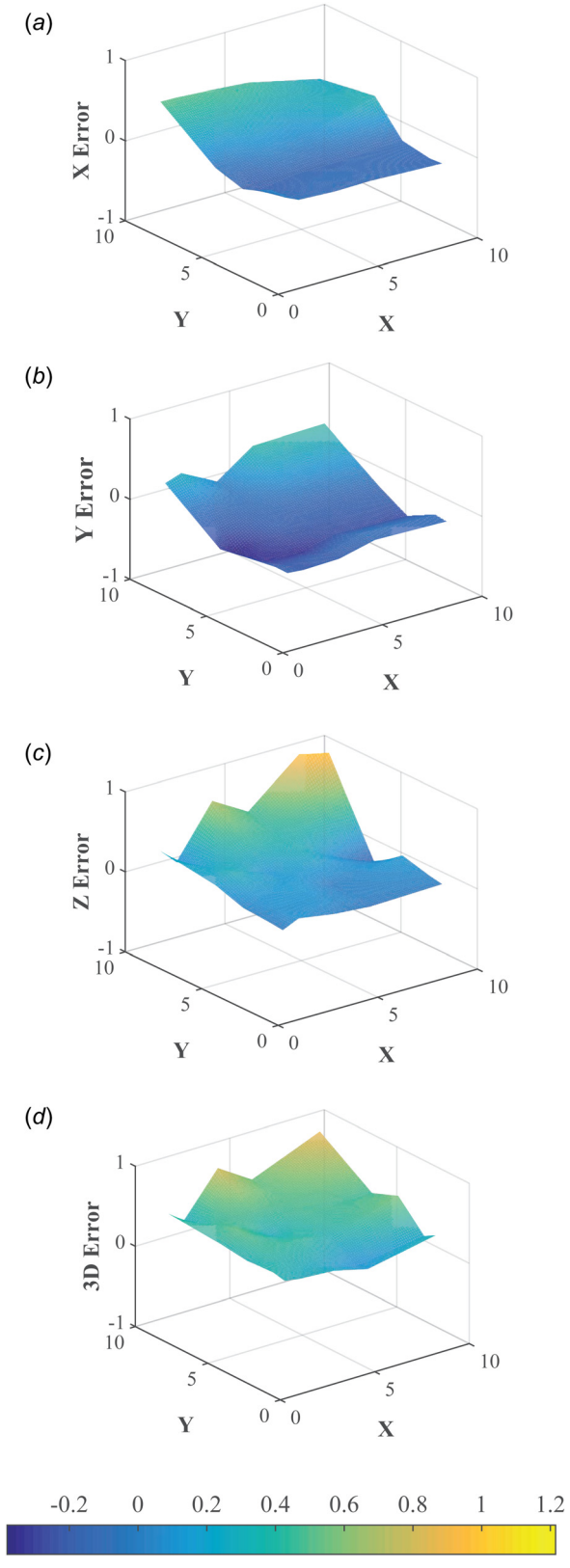

Fig. 6 Maps of mean absolute error interpolated over 25 calibration targets in (*a*) *x*, (*b*) *y*, (*c*) *z*, and (*d*) magnitude averaged across ten trials (units in millimeter). Origin corresponds to top left circle in calibration grid, and axes correspond to the global device coordinate frame.

4 Conclusions and Future Work

In this paper, we presented the design and evaluation of a robotic device for automated rodent tail vein cannulations, which are among the most commonly performed procedures in preclinical research settings. We designed the device to be substantially simplified and more compact than existing prototypes described in the literature [14–17]. This paper has focused on the mechanical design and engineering testing of the device. The results of the workspace analysis and free-space positioning experiments provide evidence that the system has the precision and accuracy required for needle insertion into tail veins as small as 0.3 mm in diameter.

The current device is designed for use in anesthetized animals. However, the described needle manipulator may be adapted for attachment to commercial animal holders and restraints to minimize the need for anesthesia, which may be undesired in some preclinical testing scenarios. Alternatively, it may be possible to

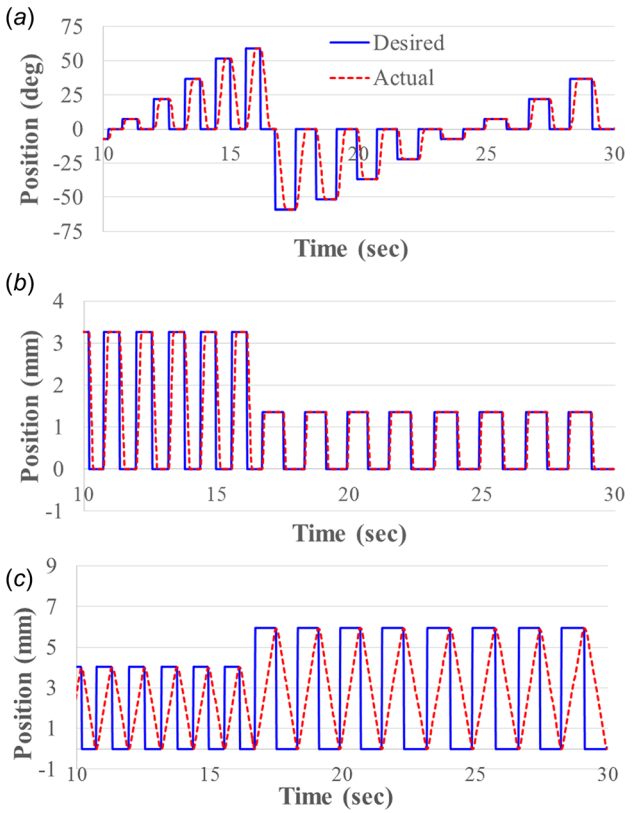

Fig. 7 Low-level motor errors during position testing over 30 s interval, showing desired (solid line) versus actual (dotted line) signals for each DOF: (*a*) θ_{FG}, (*b*) Z_{NM}, and (*c*) D_{ins}

use the device in a handheld manner, for example, by eliminating the animal platform and clipping the manipulator directly to the tail. Subsequent studies will investigate the range of potential form factors for the device. Additionally, we will implement methods to apply the needle tip offsets identified in the positioning studies as correction terms in the kinematic equations, thus compensating for systematic robot errors. If needle bending is observed during testing, using a different cannula or adjusting the angle of insertion may help resolve the issue. We will also evaluate the NIR imaging and image analysis techniques deployed in the system to determine how these processes affect tail vein visualization, segmentation, and localization.

To test these new device advancements in a systematic manner and assess the effects of animal variability on device performance, we will utilize customizable tissue-mimicking phantom models tuned to simulate the mechanical and optical properties of the rat tail and vessels. Finally, in vivo evaluations will be conducted on live rodent models to compare cannulation success rates and blood sampling repeatability to results obtained by manual techniques.

Funding Data

- National Institutes of Health (Grant Nos. EB018191, R01EB020036 and T32 GM008339).
- National Science Foundation (Grant No. DGE-0937373).
- U.S. Department of Education (Grant No. P200A150131).

Nomenclature

AoR = axis of rotation
D_{ins} = insertion motion of needle manipulator
LED = light-emitting diode
NIR = near infrared
Z_{NM} = Z-motion of needle manipulator
θ_{FG} = friction gear rotation about the X-axis

References

[1] Nolan, P. M., Peters, J., Strivens, M., Rogers, D., Hagan, J., Spurr, N., Gray, I. C., Vizor, L., Brooker, D., Whitehill, E., Washbourne, R., Hough, T., Greenaway, S., Hewitt, M., Liu, X., McCormack, S., Pickford, K., Selley, R., Wells, C., Tymowska-Lalanne, Z., Roby, P., Glenister, P., Thornton, C., Thaung, C., Stevenson, J.-A., Arkell, R., Mburu, P., Hardisty, R., Kiernan, A., Erven, A., Steel, K. P., Voegeling, S., Guenet, J.-L., Nickols, C., Sadri, R., Naase, M., Isaacs, A., Davies, K., Browne, M., Fisher, E. M., Martin, J., Rastan, S., Brown, S. D., and Hunter, J., 2000, "A Systematic, Genome-Wide, Phenotype-Driven Mutagenesis Programme for Gene Function Studies in the Mouse," Nat. Genet., **25**(4), pp. 440–443.

[2] Chang, Y.-C., Berry-Pusey, B., Yasin, R., Vu, N., Maraglia, B., Chatziioannou, A. X., and Tsao, T.-C., 2015, "An Automated Mouse Tail Vascular Access System by Vision and Pressure Feedback," IEEE/ASME Trans. Mechatronics, **20**(4), pp. 1616–1623.

[3] Springer, M. L., Sievers, R. E., Viswanathan, M. N., Yee, M. S., Foster, E., Grossman, W., and Yeghiazarians, Y., 2005, "Closed-Chest Cell Injections Into Mouse Myocardium Guided by High-Resolution Echocardiography," Am. J. Physiol.: Heart Circ. Physiol., **289**(3), pp. 1307–1314.

[4] Kanoh, K., Shimura, T., Suzuki, H., Nomoto, K., Asao, T., and Kuwano, H., 2004, "Antitumor Effect of a Splenic Injection of 5-Fluorouracil on Metastatic Liver Cancer in Mice," J. Pharmacol. Exp. Ther., **308**(1), pp. 168–174.

[5] Malakoff, D., 2000, "The Rise of the Mouse, Biomedicine's Model Mammal," Science, **288**(5464), pp. 248–253.

[6] Bebek, Ö., Hwang, M. J., and Cavusoglu, M. C., 2013, "Design of a Parallel Robot for Needle-Based Interventions on Small Animals," IEEE/ASME Trans. Mechatronics, **18**(1), pp. 62–73.

[7] Shima, H., Ohno, K., Michi, K-I., Egawa, K., and Takiguchi, R., 1996, "An Anatomical Study on the Forearm Vascular System," J. Cranio-Maxillofac. Surg., **24**(5), pp. 293–299.

[8] Staszyk, C., Bohnet, W., Gasse, H., and Hackbarth, H., 2003, "Blood Vessels of the Rat Tail: A Histological Re-Examination With Respect to Blood Vessel Puncture Methods," Lab. Anim., **37**(2), pp. 121–125.

[9] Groman, E. V., and Reinhardt, C. P., 2004, "Method to Quantify Tail Vein Injection Technique in Small Animals," J. Am. Assoc. Lab. Anim. Sci., **43**(1), pp. 35–38.

[10] Gordon, C. J., 1983, "Influence of Heating Rate on Control of Heat Loss From the Tail in Mice," Am. J. Physiol.: Regul. Integr. Comp. Physiol., **244**(6), pp. R778–R784.

[11] Berry-Pusey, B. N., 2012, "A Vascular Access System (VAS) for Preclinical Models," Ph.D. thesis, University of California, Los Angeles, CA.

[12] Singh, J., 2012, "The National Centre for the Replacement, Refinement, and Reduction of Animals in Research," J. Pharmacol. Pharmacother., **3**(1), pp. 87–89.

[13] Waspe, A. C., Lacefield, J. C., and Fenster, A., 2007, "Registration of Three-Dimensional High-Frequency Ultrasound Images to a Robotic Needle-Positioning System for Pre-Clinical Research," IEEE International Symposium on Biomedical Imaging: From Nano to Macro (ISBI), Arlington, VA, Apr. 12–15, pp. 1132–1135.

[14] Berry-Pusey, B. N., Chang, Y. C., Prince, S. W., Chu, K., David, J., Taschereau, R., Silverman, R. W., Williams, D., Ladno, W., Stout, D., Tsao, T. C., and Chatziioannou, A., 2013, "A Semi-Automated Vascular Access System for Preclinical Models," Phys. Med. Biol., **58**(16), pp. 5351–5362.

[15] Kazanzides, P., Chang, J., Iordachita, I., Li, J., Ling, C., and Fichtinger, G., 2007, "Development of an Image-Guided Robot for Small Animal Research," Comput. Aided Surg., **12**(6), pp. 357–365.

[16] Waspe, A. C., Cakiroglu, H. J., Lacefield, J. C., and Fenster, A., 2007, "Design, Calibration and Evaluation of a Robotic Needle-Positioning System for Small Animal Imaging Applications," Phys. Med. Biol., **52**(7), pp. 1863–1878.

[17] Ayadi, A., Bayle, B., Graebling, P., and Gangloff, J., 2008, "An Image-Guided Robot for Needle Insertion in Small Animal. Accurate Needle Positioning Using Visual Servoing," IEEE/RSJ International Conference on Intelligent Robots and Systems (IROS), Nice, France, Sept. 22–26, pp. 1453–1458.

[18] Chen, A. I., Balter, M. L., Maguire, T. J., and Yarmush, M. L., 2016, "3D Near Infrared and Ultrasound Imaging of Peripheral Blood Vessels for Real-Time Localization and Needle Guidance," International Conference on Medical Image Computing and Computer-Assisted Intervention (MICCAI), Quebec City, QC, Canada, Sept. 10–14, pp. 388–396.

[19] Rand, R., Burton, A., and Ing, T., 1965, "The Tail of the Rat, in Temperature Regulation and Acclimatization," Can. J. Physiol. Pharmacol., **43**(2), pp. 257–267.

[20] Heikkila, J., 2000, "Using Circular Control Points," IEEE Trans. Pattern Anal. Mach. Intell., **22**(10), pp. 1066–1077.

[21] Balter, M. L., Chen, A. I., Maguire, T. J., and Yarmush, M. L., 2017, "Adaptive Kinematic Control of a Robotic Venipuncture Device Based on Stereo Vision, Ultrasound, and Force Guidance," IEEE Trans. Ind. Electron., **64**(2), pp. 1626–1635.